A dynamic collimation and alignment system for the Helmholtz linear accelerator

Cite as: Rev. Sci. Instrum. 92, 113306 (2021); https://doi.org/10.1063/5.0069824 Submitted: 02 September 2021 • Accepted: 02 November 2021 • Published Online: 24 November 2021

🗓 S. Lauber, K. Aulenbacher, 🗓 W. Barth, et al.









ARTICLES YOU MAY BE INTERESTED IN

Extreme ultraviolet-excited time-resolved luminescence spectroscopy using an ultrafast table-top high-harmonic generation source

Review of Scientific Instruments 92, 113004 (2021); https://doi.org/10.1063/5.0064780

Beam power scale-up in micro-electromechanical systems based multi-beam ion accelerators

Review of Scientific Instruments 92, 103301 (2021); https://doi.org/10.1063/5.0058175

Swift evaluation of electron density profiles obtained by the alkali beam emission spectroscopy technique using linearized reconstruction

Review of Scientific Instruments 92, 113501 (2021); https://doi.org/10.1063/5.0057158





A dynamic collimation and alignment system for the Helmholtz linear accelerator

Cite as: Rev. Sci. Instrum. 92, 113306 (2021); doi: 10.1063/5.0069824 Submitted: 2 September 2021 • Accepted: 2 November 2021 • Published Online: 24 November 2021







AFFILIATIONS

- ¹ Helmholtz Institute Mainz, Mainz 55128, Germany
- ²GSI Helmholtz Center for Heavy Ion Research, Darmstadt 64291, Germany
- ³KPH, Johannes Gutenberg University, Mainz 55128, Germany
- ⁴IAP, Goethe University Frankfurt, Frankfurt 60438, Germany

ABSTRACT

The upcoming commissioning of the superconducting (SC) continuous wave Helmholtz linear accelerators first of series cryomodule is going to demand precise alignment of the four internal SC cavities and two SC solenoids. For optimal results, a beam-based alignment method is used to reduce the misalignment of the whole cryomodule, as well as its individual components. A symmetric beam of low transverse emittance is required for this method, which is to be formed by a collimation system. It consists of two separate plates with milled slits, aligned in the horizontal and vertical direction. The collimation system and alignment measurements are proposed, investigated, and realized. The complete setup of this system and its integration into the existing environment at the GSI High Charge State Injector are presented, as well as the results of the recent reference measurements.

© 2021 Author(s). All article content, except where otherwise noted, is licensed under a Creative Commons Attribution (CC BY) license (http://creativecommons.org/licenses/by/4.0/). https://doi.org/10.1063/5.0069824

I. INTRODUCTION

The scientific research for new Super-Heavy Elements (SHEs) performs collision experiments on fixed heavy-ion targets with medium to heavy mass projectiles. The conducted fusion evaporation reactions have extremely low cross sections, which makes stable, long-term, continuous wave operation vital for further discoveries. Therefore, a dedicated particle accelerator is being developed, which best meets those requirements.

Recently, the GSI Helmholtz Center for Heavy Ion Research extends the research fields with the construction of the large scale project FAIR (Facility for Antiproton and Ion Research at Darmstadt). For this purpose, the existing Universal Linear Accelerator (UNILAC), which supplied the SHE program with heavy ion beams, will be upgraded for high current short pulse operation as part of the injector chain for FAIR. ^{3–8}

Thus, the Helmholtz Linear Accelerator (HELIAC), dedicated to deliver beam to SHE experiments, is going to be built at GSI: a continuous wave (CW) and superconducting (SC) heavy ion accelerator with variable output energy, 9-11 consisting of a

normal-conducting injector linac and a superconducting main part, comprising four cryomodules. ¹¹ This project is realized by GSI and the Helmholtz Institute Mainz (HIM) ^{12,13} under the key support of the Goethe University Frankfurt (GUF) ^{14,15} and in collaboration with the Moscow Engineering Physics Institute (MEPhI) and the Moscow Institute for Theoretical and Experimental Physics (KI-ITEP). ^{16,17} An adoption of SC linacs is a crucial technology for various international accelerator driven research facilities, such as spallation neutron source, medium energy applications in material science, isotope generation, and boron-neutron capture therapy. Many of those ambitious accelerators strongly rely on cutting-edge engineering and accurate machining of superconducting and/or continuous wave multi-gap cavities. ^{18–26}

As the first superconducting accelerator at GSI, HELIAC adds to the list of existing and planned advanced linacs at this research center: the FAIR proton linac and UNILAC proton beam delivery, ^{27–29} the linear heavy ion decelerator HITRAP, ³⁰ and the LIGHT (Laser Ion Generation, Handling and Transport) facility for laser acceleration of protons and heavy ions. ³¹

a) Author to whom correspondence should be addressed: s.lauber@gsi.de

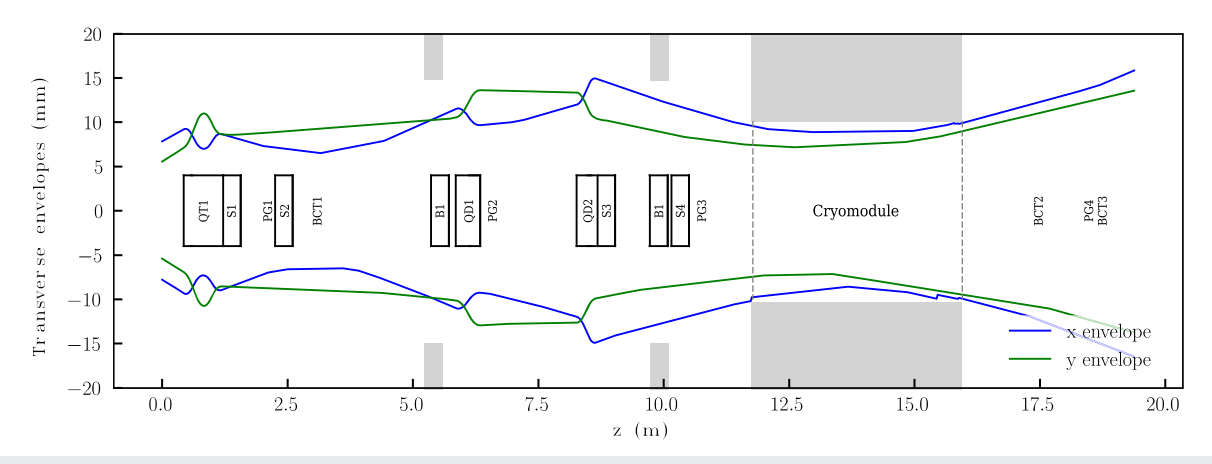


FIG. 1. Design envelopes of a 1.4 MeV/u Ar⁸⁺ beam (see Table I) from the HLI to the end of the *Advanced Demonstrator* with minor losses at the cryostat aperture. Relevant beam line components: Quadrupole Triplet (QT), Steerer (S), Profile Grid (PG), Beam Current Transformer (BCT), Quadrupole Doublet (QD), and Buncher (B). The gray blocks indicate the aperture of the external bunchers and the cavities inside the cryomodule.

Previous project milestones, such as the cold test of three SC crossbar H-mode bar H-mode (CH) resonators and the beam test of the first f the series SC resonator on a dedicated test bench beamline, the so-called demonstrator, have already been completed. 9,32 The heavy ion beam with 1.4 MeV/u energy is provided by the existing High Charge State Injector, one of the two GSI injector linacs. 33-35 In the future, it is foreseen to build a dedicated CW injector with its own matching beam line.

The next R & D stages are the cold test of a new cryostat with the beam. The cryostat is going to be equipped with four dummy cavities, which will be substituted with the actual SC CH cavities later on. This will be realized in the same but upgraded beam line, the so-called *Advanced Demonstrator*. Because of the upgrade, numerous beam line elements have been relocated and the new cryomodule has been installed (see Fig. 1). Therefore, the alignment of all elements has to be checked, which is well known routine operation for a normal conducting section. Various beam diagnostic methods are available for the subsequent analysis of the beam. ^{36–44}

However, the cavities inside the assembled cryostat are not accessible for conventional alignment methods. The cavities potentially change their position and orientation with the cool-down from room temperature to the operating temperature of 4 K. However, due to the technical design features of the cryostat, even after cooldown, the cavities can be realigned externally by adjusting their suspension strings. To investigate the displacement of the components in the cryostat (especially during beam commissioning), it was proposed to use a symmetric, parallel beam of low transverse emittance, i.e., pencil-like, to scan/raster the aperture using beam steerers. The obtained spatial information on the effective aperture can then be used to profile the misalignment and as guidance for the alignment team. A beam with higher emittance would otherwise distort and blur the raster imaging. In general, an application of a collimation system is useful for machine investigation, further beam line optimization and safe routine operation. Therefore, it is widely implemented at different accelerator facilities worldwide.45-51

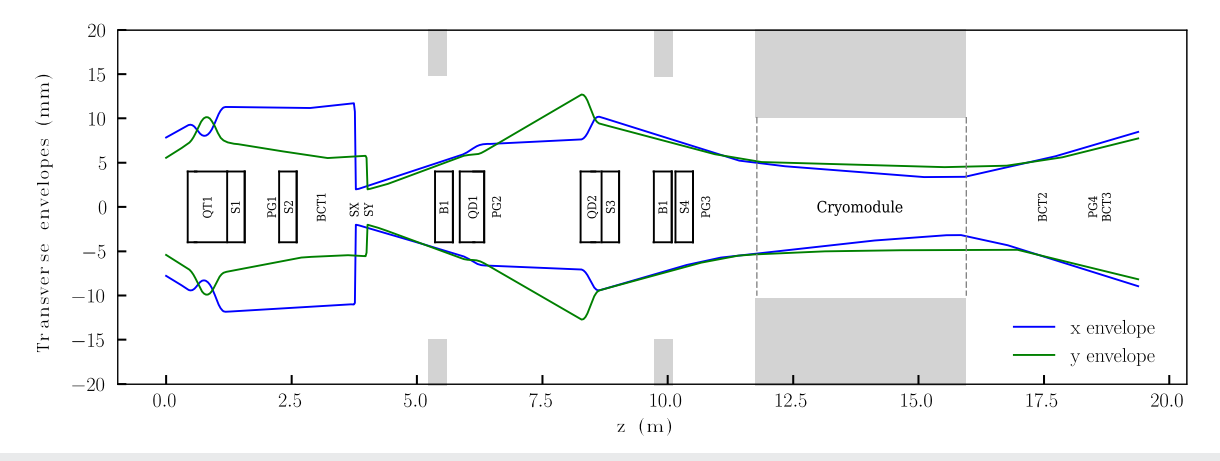


FIG. 2. Design envelopes with collimation of a 1.4 MeV/u Ar⁸⁺ beam (see Table I) from the HLI to the end of the *Advanced Demonstrator*. Relevant beam line components: Quadrupole Triplet (QT), Steerer (S), Profile Grid (PG), Beam Current Transformer (BCT), Horizontal–Vertical Slit (SX/SY), Quadrupole Doublet (QD), and Buncher (B). The gray blocks indicate the aperture of the external bunchers and the cavities inside the cryomodule.

The pencil-like beam is shaped at the HELIAC Advanced Demonstrator with a collimation system to be as thin as possible along the whole cryostat (see Fig. 2). Two grounded plates with slits, oriented correspondingly in the horizontal and vertical direction, should cut a part of the transverse spatial particle distribution, providing for a small beam spot with low divergence downstream the slits. Due to limited space, an originally foreseen second pair of slits is not implemented. Thus, the system is more compact and particularly user-friendly, as only two instead of four step motors have to be controlled. The geometric dimensions of the slits and the corresponding quadrupole settings were defined by simulation in advance (see Sec. II). Moreover, the collimation system is foreseen for the alignment of the cavities with low beam current, duty cycle, and short pulsed beam. It is not intended to use this system during high beam power operation. During the technical construction of the collimation system, it must be ensured that the thermal load, induced by the beam loss, does not cause significant damage to the slit plates (see Sec. III). Finally, reference emittance and transmission measurements of the pencil-like beam are presented, as well as effective aperture measurements employing the collimated beam (see Sec. IV).

II. COLLIMATOR DESIGN AND REFERENCE BEAM DYNAMICS

As it is intended to scan the apertures of the cavities inside the cryomodule applying a symmetric beam of low transverse emittance, the beam size has to be optimized for a minimal diameter along the whole cryostat. The slits, aligned in the horizontal and vertical direction, are milled on two separate plates and are located after the first quadrupole triplet. In order to design the collimation system, beam dynamics simulations were carried out, using the multi-particle code DYNAMION.⁵² Space charge effects are not relevant in this setup due to the low beam current below 50 μ A. Even for the higher beam current of 1 mA, it has been demonstrated that the beam current has minor influence on the beam dynamics.¹¹ The initial particle distribution has been defined using emittance measurements, obtained in a former measurement campaign.⁵³ A transverse 4D-Waterbag distribution, reflecting these measurements, is used (see Table I). The low coupling between transverse and longitudinal particle motion in 6D phase space in our setup allows us to set to the longitudinal phase and energy spread to zero.

One quadrupole triplet and two quadrupole doublets, as well as a pair of slits, used for collimation, are considered (see Fig. 2) for the calculations of the particle trajectories. All seven quadrupole gradients and the slit width are the parameters of interest.

To find the optimal slit geometry and corresponding quadrupole gradients, dedicated software has been developed in order to minimize the transverse beam size and divergence within the cryomodule and at the last profile grid PG4 by choosing quadrupole gradients. The optimization is performed with assistance of the Nelder–Mead algorithm, ⁵⁴ which generally minimizes a function $f(\vec{g})$.

A custom performance function was developed to address our requirements for the system:

- a narrow beam along the whole cryostat [Eq. (2)],
- an overall medium beam size to stay inside the linear region of the quadrupoles [Eq. (3)],

TABLE I. Design specifications and input parameters for beam dynamics simulation. 53

Parameter	Value
RF-frequency f ₀	108.408 MHz
Mass to charge ratio	6
Beam current I	50 μA
Beam duty factor	0.025% (25%)
Input beam energy E_0	1.4 MeV/u
Particle distribution type	4D-Waterbag
Horizontal twiss parameters	
α_{x}	-1.16
β_x	3.04 mm/mrad
\mathcal{E}_{x}	18.79 mm mrad
Vertical twiss parameters	
α_{v}	-1.64
β_{ν}	2.49 mm/mrad
ε_{y}	11.4 mm mrad

- full transmission operation [only intentional losses at the slits are allowed, Eq. (4)],
- a symmetric beam inside the cryostat.

The procedural optimization to fulfill these goals can be divided into the following steps:

- 1. Set quadrupole gradients \vec{g} according to the Nelder–Mead algorithm.
- 2. Calculate beam dynamics and yield trajectories $\vec{x}(\vec{g})$ and $\vec{y}(\vec{g})$ until slits
- 3. Sweep and set slit width to set desired transmission.
- 4. Calculate the cut particle ensemble until the end of the line.
- 5. Calculate the performance function f [Eq. (1)].
- 6. Report *f* to Nelder–Mead and go to 1 until convergence.

This yields the optimal [in terms of $f(\vec{g})$] combination of quadrupole gradients and slit widths. The performance function $f(\vec{g})$ [see Eq. (1)], depending on the set of quadrupole gradients \vec{g} and the resulting particle horizontal $\vec{x}(\vec{g})$ and vertical $\vec{y}(\vec{g})$ trajectories, is used for optimization and consists of the following three measures, generally depending on the one-dimensional particle trajectory \vec{u} as a placeholder. They are designed to deliver a value of 0 if the design criteria are met and a value ≤ 1 when the target is missed but is within a tolerance margin t_i . Values higher than the tolerance inflict a quadratic penalty. The performance function is

$$f(\vec{g}) = f_1(\vec{x}_{cry}) + f_1(\vec{y}_{cry}) + |f_1(\vec{x}_{cry}) - f_1(\vec{y}_{cry})| + f_2(\vec{x}) + f_2(\vec{y}) + f_3(\vec{x}),$$
(1)

$$f_1(\vec{u}(\vec{g})) = \left(\frac{\max(\vec{u})}{t_1}\right)^2,\tag{2}$$

$$f_2(\vec{u}(\vec{g})) = \left(\frac{\max(\vec{u}) - u_{\text{target}}}{t_2}\right)^2,\tag{3}$$

$$f_3(\vec{u}(\vec{g})) = \left(\frac{\text{transmission}(\vec{u}) - t_{\text{target}}}{t_3}\right)^2,$$
 (4)

where x_{cry} and y_{cry} are the sub-selections of the trajectories inside the cryostat. The function f_1 is used to minimize the transverse beam size inside the cryostat for the lowest size with a tolerance parameter of $t_1 = 2$ mm.

The term $|f_1(\vec{x}_{\text{cry}}) - f_1(\vec{y}_{\text{cry}})|$ aims for the equal beam size in the horizontal and vertical direction, effectively forcing a symmetric beam inside the cryostat. The function f_2 minimizes the overall beam size in order to stay within the quadrupole linear part of the field and targets $u_{\text{target}} = 7$ mm with a tolerance of $t_2 = 1$ mm. This is a rather arbitrary choice but has proven to provide for better balancing between the multiple objectives. Another choice could have been a higher target with lower tolerance like $u_{\text{target}} = 12$ mm and $t_2 = 0.3$ mm, which on the other hand would have altered the quadratic behavior of the target function and lead to interference with the other objective functions.

The function f_3 accounts for the particle transmission and handles additional losses to those at the collimator, which may be caused by the minimum aperture radius of 10 mm along the cryostat. This must be considered to prevent the algorithm from unintentionally scraping a part of the beam at a location other than the slits, which would result in a smaller beam size, beneficial to the other objectives.

In order to provide for a beam current measurement accuracy of 10%, a reasonable lower limit for the beam current is assumed as $10~\mu A$ due to a beam current measurement accuracy of $\pm 1~\mu A$. With an anticipated and commonly delivered beam current of $50~\mu A$, a particle transmission through the slits of $t_{\rm target} = 20\%$ is targeted with a tolerance of $t_3 = 2\%$.

To consider the maximum quadrupole gradients, another performance criterion f_4 could have been included. However, the algorithm did converge to realistic gradients. It was decided to omit f_4 in favor of low complexity.

For each beam dynamics simulation run, the slit width is dynamically adjusted. For this purpose, the particle ensemble is calculated forward until the slit. Then, the slit width is adjusted so that the targeted losses occur at the slit. The cut particle ensemble is then tracked to the end of the beam line. The performance function is finally evaluated as a post-process. As the slit widths are inferenced indirectly, the parameter search space is reduced and allows for an efficient run-time of the software. The best set of quadrupole gradients in terms of $f(\vec{g})$ implicitly yields the appropriate slit width

An exemplary application of the optimization algorithm is shown in Fig. 3. In general, the specific convergence shape strongly depends on the starting point of optimization and the specific beam line layout, as well as the parametrization of the performance function.

With the presumed input distribution, two quadrupole settings are prepared for operation: one set up without slits and one to operate with slits (see Table II).

Without slits, the quadrupole settings were additionally optimized for minimal beam loss. The target transmission parameter is temporally assigned to $t_{\rm target} = 100\%$. The main source of the beam loss is the tight aperture radius of 10 mm inside the cryomodule (see Fig. 1). Two SC solenoids will be operated in the future to allow for a different focusing scheme with full transmission. However, the use

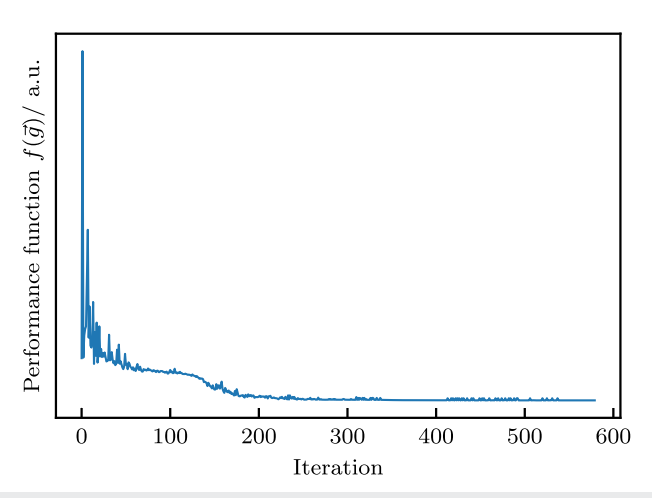


FIG. 3. Minimization of the performance function $f(\vec{g})$, applying the Nelder–Mead algorithm.

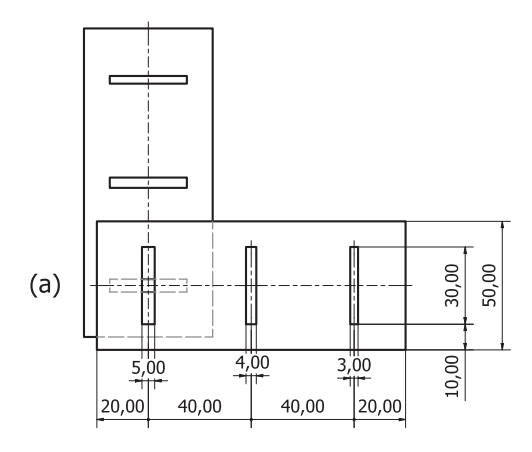
of solenoids during the aperture scan potentially leads to a dramatic perturbation of the pencil-beam, including undesired steering.

With slits, the optimization yields a slit half-width of 1.93 mm, so that a main slit half-width of 2 mm is defined for practical reasons. By using a slit half-width of 2 mm and the corresponding quadrupole gradients, the beam transmission is set to 20%, keeping the horizontal and vertical envelopes inside the cryomodule as thin as possible, also with a small beam spot at the profile grid PG4 at the end of the line (see Fig. 2). In this simulation, all losses are caused by the slits and no further aperture is hit. To deal with different beam parameters (current, emittance, etc.) for different ion species during operation of the collimation system, two additional slits of 1.5 and 2.5 mm are milled in the same plate [see Fig. 4(a)]. These two additional slits are not selected by optimization but manually to provide the reasonable adaptability of the beam parameters (see Tables III and IV).

The combination of the different slit widths on one plate results in an adjustable transmission during operation, without the necessity to change the quadrupole parameters, as shown in Table III. As a consequence of the independent selection of the slit size per plate, the horizontal and vertical beam emittances ε_x and ε_y behind the slits are set separately by the chosen slit width combination to provide for a symmetric beam (see Table IV). The variable transmission is especially useful to further limit the beam size if the beam current

TABLE II. Quadrupole design gradients proposed for operation.

Quadrupole	Gradient (T/m) without slits	Gradient (T/m) 2.0 mm slit half-width
QT11	9.7	7.2
QT12	-8.6	-8.4
QT13	7.8	8.3
QD11	4.4	-1.6
QD12	-4.1	2.5
QD21	-6.1	-9.5
QD22	6.7	8.9



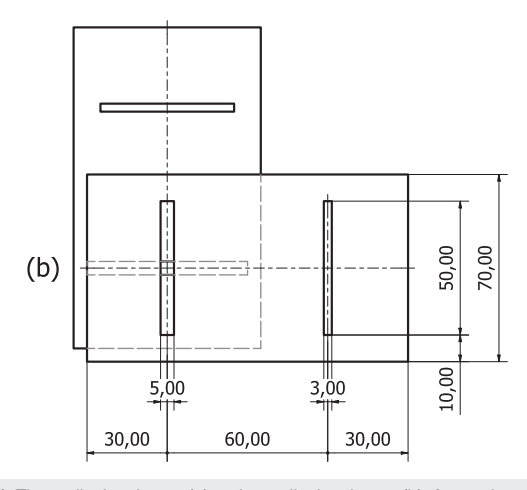


FIG. 4. Three-slit plate layout (a) and two-slit plate layout (b); 2 mm plate depth.

surpasses the detection limit. An insufficient measured beam current is counteracted by using wider slits, yielding a higher particle transmission.

The described three slits layout allows for a high flexibility during operation but potentially carries the risk that particles bypass the plate on unintended trajectories (through a neighboring slit or past the plate) if the transverse beam size and divergence are significantly higher than anticipated. Even though the simulations at eight times the transverse design emittance could not prove any undesirable effects, another two-slit plate layout is designed and produced, which uses only two slits per plate. An enlarged distance between

TABLE III. Simulated transmission for combinations of different slit half-widths.

		Horizontal		
Slit half-width		2.5 mm	2.0 mm	1.5 mm
Vertical	2.5 mm 2.0 mm 1.5 mm	29.0% 23.4% 17.7%	24.3% 19.7% 14.9%	19.1% 15.6% 11.7%

TABLE IV. Simulated emittances $\varepsilon_{\chi}/\varepsilon_{\gamma}$ (mm mrad) at the end of the line after cutting for combinations of different slit widths.

			Horizontal	
Slit half-width		2.5 mm	2.0 mm	1.5 mm
Vertical	2.5 mm 2.0 mm 1.5 mm	6.3/7.4 6.2/6.1 6.1/4.5	5.2/7.4 5.0/6.2 5.1/4.4	3.8/7.4 3.8/6.1 3.9/4.4

the slits and the edge of the plate is achieved, reducing the probability for particles to bypass the slit-system [see Fig. 4(b)]. As the slit width is on the order of a few mm, beam scattering at the slits is negligible. The slits are not planned for routine CW operation. Thus, the incident beam current is not foreseen to be measured on the plates during operation of the collimation system for cavity realignment because a low beam current for safe operation of the slits is specified (50 $\mu\rm A$ is implemented with 0.025% duty cycle). Additionally, the adjacent beam current monitors provide transmission measurements.

III. THERMAL LOAD

To decide whether the collimation system requires to be cooled or not, the plate design is studied from a thermal point of view. With the anticipated beam current of 50 μ A, a duty cycle of 25%, and a complete loss of the beam, the mean dissipated current $I_{\rm loss}$ is up to 12.5 μ A. This results in an average power dissipation $P_{\rm loss}$ on the split plates,

$$P_{\text{loss}} = E_{\text{kin}} \cdot \frac{I_{\text{loss}}}{O \cdot e}.$$
 (5)

Therefore, the dissipated power $P_{\rm loss}$ of a 1.4 MeV/u Ar⁹⁺ ion beam is in this worst case scenario up to 80 W. However, it is intended to use the collimation system only during injector operation at a lowerd repetition rate of 2.5 Hz and a macro-bunch length of 100 s, which is routinely used to protect the beam profile grids from damage. For this scenario, the duty cycle is 0.025% and the maximum dissipated power is $P_{\rm loss} \approx 80$ mW.

For both scenarios, the results of a thermal simulation with CST^{55} (see Fig. 5) were compared to an analytical calculation, where a stainless steel block in vacuum is heated by the beam and cooled by the emission of black-body radiation. A key difference between the two calculations is the temperature distribution on the plate. While

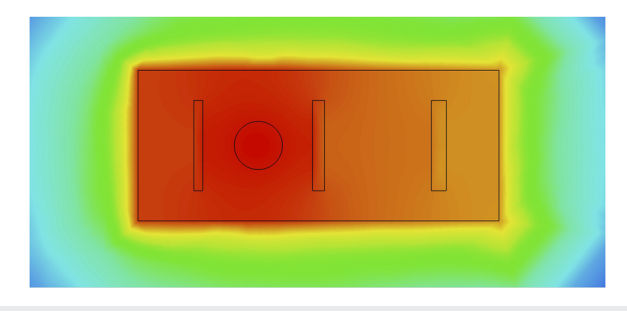


FIG. 5. Temperature distribution on the plate for $P_{loss} \approx$ 80 mW. The colors indicate temperatures from 290 to 300 K.

the algebraic approach assumes uniform heating, an incident beam spot can be specified in CST. This leads to higher peak temperatures. The heat of the stainless steel block changes corresponding to

$$\frac{\delta Q}{\delta t} = P_{\rm loss} - \varepsilon \sigma A T^4, \tag{6}$$

with the emissivity factor ε , the Stefan–Boltzmann constant σ , the surface area A, and the temperature T. The ion penetration depth is estimated from the Bethe–Bloch formula and is below $10~\mu m$. Therefore, losses are considered all on the surface. For the intended use of the plate applying a beam duty factor of 0.025%, the plate is heated by $\Delta T = 10~\rm K$, which is tolerable for long term operation. The saturation temperature is dominated by the emissivity ε , which varies by production parameters from $\varepsilon_{\rm polished} = 0.075$ to $\varepsilon_{\rm rolled} = 0.85$. The lower emissivity is chosen as the worst case scenario. An incorrect application of the collimation system during continuous wave operation could damage the plate by heat with ΔT of 500–1400 K, depending on the emissivity.

IV. COMMISSIONING

During commissioning of the upgraded beam line, the High Charge State Injector delivered about 50 μ A 40 Ar $^{+8}$ beam current. The quadrupole and steerer gradients were optimized for maximum transmission along the beam line (see Fig. 1), yielding a beam transmission of 94%, which was well predicted by beam dynamics simulations in advance. These minor losses appeared at two mounted diaphragms of 11 mm aperture radius, which emulated the presence of the *Advanced Demonstrator* cryomodule at its entry and exit point 4 m apart. To introduce a misalignment, one diaphragm was intentionally shifted vertically during assembly.

A transverse emittance measurement has been carried out at the end of the line (see Fig. 6). The slit-grid emittance measurement bench MobEmi⁵⁶ was used. Following previous experience, we estimate the measurement accuracy of emittance as 5%. The measured beam phase portrait was traced back to the start of the beam line to be compared with the originally assumed input distribution. The main twiss parameters are in sufficient agreement (see Table V). The beam width differs by 30% from the design assumptions, which is caused by different settings in the HLI injector compared to the former measurement campaign.⁵³ However, this deviation in beam width between the design assumptions and the actual values was corrected with the first quadrupole triplet QT1. The actual emittance value of the ellipse, which encloses 90% of the particles, matched nicely to the assumed transverse design beam emittance. Nevertheless, the real density pattern is rather complex and tends to be more concentrated in the center than the assumed 4D-Waterbag

The fabricated three-slits plates, mounted each on a separate stepper motor (see Fig. 7), were installed to the beam line. By investigating the beam parameters with different combinations of vertical and horizontal slits, a higher transmission (see Table VI) and a lower transverse beam emittance (see Fig. 8) compared to the simulations are observed, from which a higher signal-to-noise ratio for the beam diagnostic devices can be concluded. With slight adjustments of the quadrupole triplet QT1, a round beam could be produced using the small slits, referred to as *optimized* setting. The beam orientation at the slits was adjusted so that the same emittance is measured behind

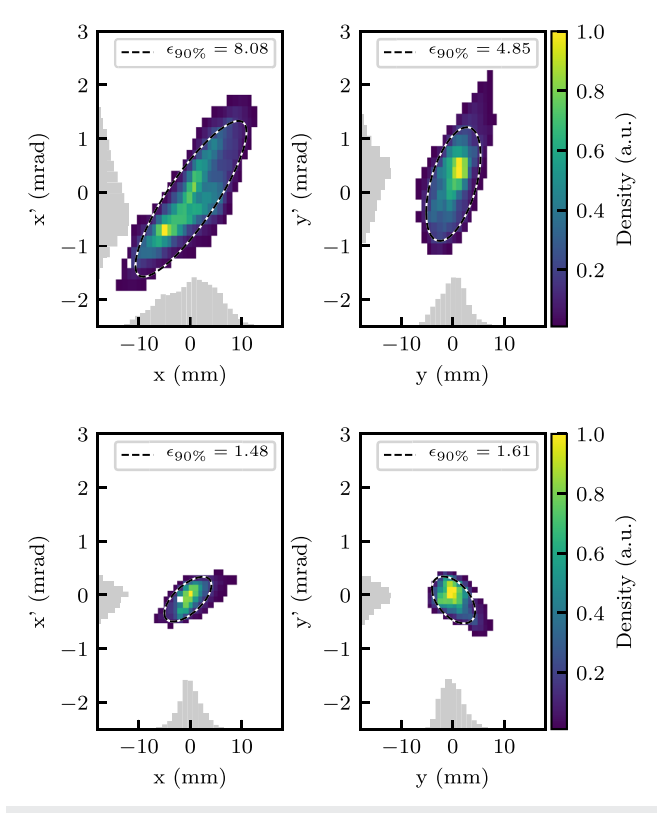


FIG. 6. Transverse beam emittance measurements at the end of the line without (top) and with (bottom) collimation. The ellipses enclose 90% of the particles.

the collimator in both planes, although the input beam has significantly different emittances in the horizontal and vertical planes (see Fig. 8). The actual emittance with the *optimized* setting is lower by a factor of 2 than foreseen by the simulations. As a consequence of the emittance measurements, a narrow beam can be expected for the upcoming beam based investigations.

TABLE V. HLI output beam parameters during the recent measurement campaign.

Parameter	Value
Ion species	⁴⁰ Ar ⁺⁸
Mass to charge ratio	5
Beam current I_{mean}	50 μA
Beam energy E_0	1.4 MeV/u
Horizontal twiss para	ameters
α_x	-1.13 ± 0.05
β_x	1.43 ± 0.04 mm/mrad
ε_{x}	$17.3 \pm 0.9 \text{ mm mrad}$
Vertical twiss parar	neters
α_y	-1.51 ± 0.07
$\beta_y^{'}$	1.39 ± 0.03 mm/mrad
$\frac{\varepsilon_y}{\varepsilon_y}$	11.5 ± 0.6 mm mrad



FIG. 7. Three-slit plate mounted on a separate stepper motor to be installed to the beam line

TABLE VI. Measured transmission for combinations of different slit half-widths.

		Horizontal		
Slit half-width		2.5 mm	2.0 mm	1.5 mm
Vertical	2.0 mm	$34.0\pm0.3\%$	$31.5 \pm 0.3\%$ $27.0 \pm 0.4\%$ $23.3 \pm 0.5\%$	$19.0 \pm 0.7\%$

With the optimized pencil-like beam, a precise scanning of the effective aperture along the cryostat is possible. For this purpose, the beam was shifted parallel to the off-axis using two beam steerers. The transverse beam offset was monitored with two beam profile grids PG3/PG4: one in front of and one behind the cryomodule. The beam current behind the cryostat was monitored for different transverse beam offsets. The effective aperture diameter is calculated as

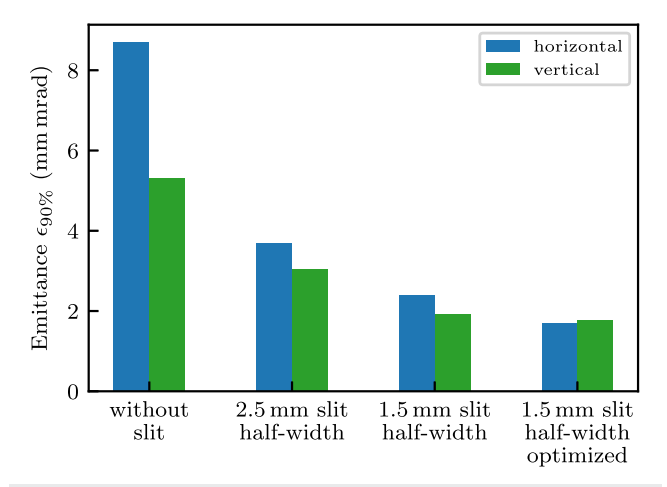


FIG. 8. Comparison of transverse beam emittance with varied levels of collimation.

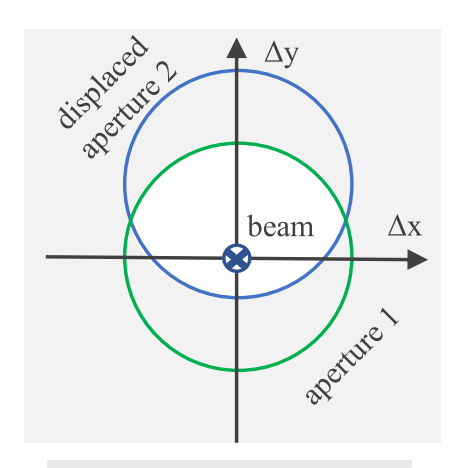


FIG. 9. Beam based effective aperture scan.

the difference between two beam offsets showing half of the maximum transmission, which both indicate that the beam is centered on the edge of the aperture and therefore half of the beam is lost.

To emulate misalignment, the investigated diaphragm was intentionally displaced vertically when being mounted. Due to the misalignment, a lower effective aperture is expected, which is caused by the intersection of the two circular apertures of 11 mm radius, as shown in Fig. 9. This intersection is of a biconvex shape and can yield a significantly reduced effective aperture in both directions, even though only a one directional aperture shift is introduced. Two series of measurements have been performed along the horizontal Δx and vertical Δy centered axis. The results of this measurement series are depicted in Fig. 10. The unsharp border on the left side of the vertical measurement emerges because the two diaphragms are longitudinally 4 m apart and only one of the apertures can be close to the beam focus to produce a sharp image. A misalignment is

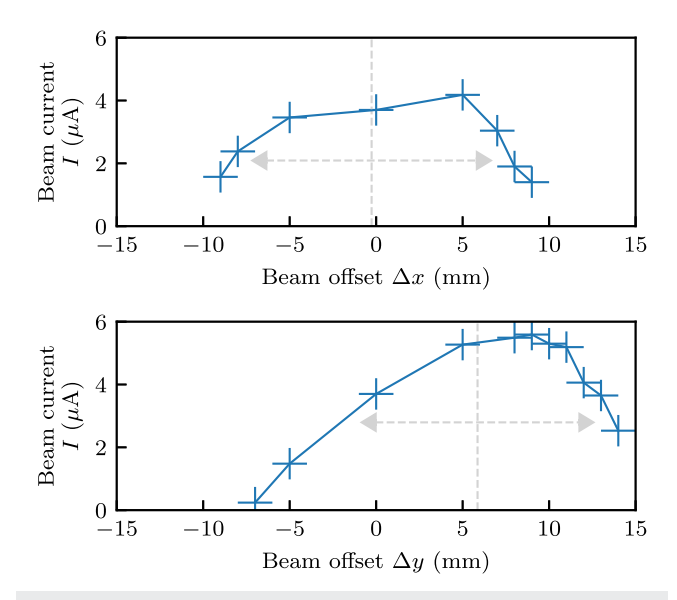


FIG. 10. Horizontal and vertical scan (with error bars) for the cryomodule with a pencil-like beam.

clearly detected, centered at $y_{\rm center}=5.8\pm2$ mm in the vertical direction and $x_{\rm center}=-0.1\pm2$ mm in the vertical direction, reducing the effective vertical aperture radius to $r_y=8.1\pm2$ mm and the horizontal one to $r_x=8.5\pm2$ mm. Since the biconvex-center and the beam axis do not have the same center, a lower effective aperture is measured for $I(\Delta x)|_{y=0{\rm mm}}$ than would have been found for $I(\Delta x)|_{y=6{\rm mm}}$. The measurement precision is limited by the distance of the profile wires in the beam profile grids. If necessary, the accuracy could be improved to less than 1 mm using beam position monitors instead of beam profile grids. Therefore, this scanning procedure is well suited and foreseen to detect the alignment of the dummy cavities and the actual cavities in the upcoming commissioning runs.

V. CONCLUSION

A new collimation system for the heavy ion CW SC 1.4 MeV/u HELIAC Advanced Demonstrator has been designed, fabricated, and successfully commissioned. It provides for a thin transverse beam of low divergence (pencil-like), with an emittance in the region of only 2 mm mrad. This corresponds to a cut of 90% of the initial beam emittance. The process of beam based alignment has been demonstrated with test diaphragms and is foreseen to be used for the alignment of the superconducting cavities inside the HELIAC cryomodules. Due to the advanced technical design of the cryomodule, the realignment of the cavities in the cold state is possible during commissioning with the beam. The presented beam collimation system is a powerful tool to allow for sophisticated machine investigations with a pencil-like beam and therefore could be of high interest for the accelerator community, especially for superconducting machines.

ACKNOWLEDGMENTS

The authors would like to acknowledge the GSI Beam Instrumentation Department for support and kind and productive cooperation.

AUTHOR DECLARATIONS

Conflict of Interest

The authors have no conflicts to disclose.

DATA AVAILABILITY

The data that support the findings of this study are available from the corresponding author upon reasonable request.

REFERENCES

- ¹M. Block, D. Ackermann, K. Blaum, C. Droese, M. Dworschak, S. Eliseev, T. Fleckenstein, E. Haettner, F. Herfurth, F. P. Heßberger *et al.*, "Direct mass measurements above uranium bridge the gap to the island of stability," Nature **463**, 785–788 (2010).
- ²J. Khuyagbaatar, A. Yakushev, C. E. Düllmann, D. Ackermann, L.-L. Andersson, M. Asai, M. Block, R. A. Boll, H. Brand, D. M. Cox *et al.*, "Search for elements 119 and 120," Phys. Rev. C **102**, 064602 (2020).
- ³W. Barth, W. Bayer, L. Dahl, L. Groening, S. Richter, and S. Yaramyshev, "Upgrade program of the high current heavy ion UNILAC as an injector for FAIR," Nucl. Instrum. Methods Phys. Res., Sect. A 577, 211–214 (2007).

- ⁴W. Barth, A. Adonin, C. Düllmann, M. Heilmann, R. Hollinger, E. Jäger, O. Kester, J. Khuyagbaatar, J. Krier, E. Plechov *et al.*, "High brilliance uranium beams for the GSI FAIR," Phys. Rev. Accel. Beams **20**, 050101 (2017).
- ⁵L. Groening, W. Barth, W. Bayer, G. Clemente, L. Dahl, P. Forck, P. Gerhard, I. Hofmann, G. Riehl, S. Yaramyshev *et al.*, "Benchmarking of measurement and simulation of transverse rms-emittance growth," Phys. Rev. Spec. Top.-Accel. Beams 11, 094201 (2008).
- ⁶W. Barth, A. Adonin, C. E. Düllmann, M. Heilmann, R. Hollinger, E. Jäger, J. Khuyagbaatar, J. Krier, P. Scharrer, H. Vormann *et al.*, "U²⁸⁺-intensity record applying a H₂-gas stripper cell," Phys. Rev. Spec. Top.-Accel. Beams **18**, 040101 (2015).
- ⁷A. A. Adonin and R. Hollinger, "Beam brilliance investigation of high current ion beams at GSI heavy ion accelerator facility," Rev. Sci. Instrum. **85**, 02A727 (2014).
- ⁸S. Yaramyshev, H. Vormann, A. Adonin, W. Barth, L. Dahl, P. Gerhard, L. Groening, R. Hollinger, M. Maier, S. Mickat *et al.*, "Virtual charge state separator as an advanced tool coupling measurements and simulations," Phys. Rev. Spec. Top.-Accel. Beams 18, 050103 (2015).
- ⁹W. Barth, K. Aulenbacher, M. Basten, M. Busch, F. Dziuba, V. Gettmann, M. Heilmann, T. Kürzeder, M. Miski-Oglu, H. Podlech *et al.*, "First heavy ion beam tests with a superconducting multigap CH cavity," Phys. Rev. Accel. Beams 21, 020102 (2018).
- ¹⁰ W. Barth, K. Aulenbacher, M. Basten, F. Dziuba, V. Gettmann, M. Miski-Oglu, H. Podlech, and S. Yaramyshev, "A superconducting CW-LINAC for heavy ion acceleration at GSIX," EPJ Web Conf. 138, 01026 (2017).
- ¹¹M. Schwarz, S. Yaramyshev, K. Aulenbacher, W. Barth, M. Basten, M. Busch, C. Burandt, T. Conrad, F. Dziuba, V. Gettmann *et al.*, "Reference beam dynamics layout for the SC CW heavy ion HELIAC at GSI," Nucl. Instrum. Methods Phys. Res., Sect. A **951**, 163044 (2019).
- ¹²W. Barth, K. Aulenbacher, M. Basten, M. Busch, F. Dziuba, V. Gettmann, M. Heilmann, T. Kurzeder, M. Miski-Oglu, H. Podlech *et al.*, "Superconducting CH-cavity heavy ion beam testing at GSI," J. Phys.: Conf. Ser. **1067**, 052007 (2018).
- ¹³F. Dziuba, K. Aulenbacher, W. Barth, M. Basten, C. Burandt, M. Busch, T. Conrad, V. Gettmann, M. Heilmann, T. Kürzeder *et al.*, "Further RF measurements on the superconducting 217 MHz CH demonstrator cavity for a CW linac at GSI," J. Phys.: Conf. Ser. **1350**, 012185 (2019).
- 14 S. Minaev, U. Ratzinger, H. Podlech, M. Busch, and W. Barth, "Superconducting, energy variable heavy ion linac with constant β, multicell cavities of CH-type," Phys. Rev. Spec. Top.-Accel. Beams 12, 120101 (2009).
- ¹⁵H. Podlech, U. Ratzinger, H. Klein, C. Commenda, H. Liebermann, and A. Sauer, "Superconducting CH structure," Phys. Rev. Spec. Top.-Accel. Beams 10, 080101 (2007).
- ¹⁶ M. Gusarova, W. A. Barth, S. Yaramyshev, M. Miski-Oglu, M. Basten, and M. Busch, "Design of the two-gap superconducting re-buncher," J. Phys.: Conf. Ser. 1067, 082005 (2018).
- ¹⁷ K. Taletskiy, M. Gusarova, W. A. Barth, M. Basten, M. Busch, M. Miski-Oglu, and S. Yaramyshev, "Comparative study of low beta multi-gap superconducting bunchers," J. Phys.: Conf. Ser. 1067, 082006 (2018).
- ¹⁸S. M. Polozov and A. D. Fertman, "High-energy proton beam accelerators for subcritical nuclear reactors," At. Energ. 113, 192–200 (2013).
- ¹⁹Z.-J. Wang, Y. He, H. Jia, W.-p. Dou, W.-l. Chen, X. L. Zhang, S.-h. Liu, C. Feng, Y. Tao, W.-s. Wang *et al.*, "Beam commissioning for a superconducting proton linac," Phys. Rev. Accel. Beams **19**, 120101 (2016).
- ²⁰ I. Mardor, O. Aviv, M. Avrigeanu, D. Berkovits, A. Dahan, T. Dickel, I. Eliyahu, M. Gai, I. Gavish-Segev, S. Halfon *et al.*, "The Soreq Applied Research Accelerator Facility (SARAF): Overview, research programs and future plans," Eur. Phys. J. A 54, 91 (2018).
- ²¹ L. V. Grigorenko, B. Y. Sharkov, A. S. Fomichev, A. L. Barabanov, W. Bart, A. A. Bezbakh, S. L. Bogomolov, M. S. Golovkov, A. V. Gorshkov, and S. N. Dmitriev, "Scientific program of DERICA—Prospective accelerator and storage ring facility for radioactive ion beam research," Phys.-Usp. 62, 675–690 (2019).
- ²²Y. Iwata, S. Yamada, T. Murakami, T. Fujimoto, T. Fujisawa, H. Ogawa, N. Miyahara, K. Yamamoto, S. Hojo, Y. Sakamoto *et al.*, "Performance of a compact injector for heavy-ion medical accelerators," Nucl. Instrum. Methods Phys. Res., Sect. A 572, 1007–1021 (2007).

- ²³ R. E. Laxdal, K. Fong, M. Laverty, A. Mitra, R. Poirier, I. Sekachev, and V. Zvyagintsev, "Recent progress in the superconducting RF program at TRIUMF/ISAC," Physica C 441, 13–20 (2006).
- ²⁴ A. E. Aksent'ev, K. A. Aliev, I. A. Ashanin, Y. A. Bashmakov, A. A. Blinnikov, T. V. Bondarenko, O. L. Verzhbitskii, M. A. Gusarova, A. N. Didenko, M. S. Dmitriev *et al.*, "Modeling of proton beam dynamics in an accelerator-driver at 600-1000 meV and investigation of the electrodynamic characteristics of accelerating cavities," At. Energy 117, 347–356 (2015).
- ²⁵F. Dziuba, M. Busch, M. Amberg, H. Podlech, C. Zhang, H. Klein, W. Barth, and U. Ratzinger, "Development of superconducting crossbar-*H*-mode cavities for proton and ion accelerators," Phys. Rev. Spec. Top.-Accel. Beams **13**, 041302 (2010).
- ²⁶G. Clemente, U. Ratzinger, H. Podlech, L. Groening, R. Brodhage, and W. Barth, "Development of room temperature crossbar-*H*-mode cavities for proton and ion acceleration in the low to medium beta range," Phys. Rev. Spec. Top.-Accel. Beams 14, 110101 (2011).
- ²⁷R. Berezov, O. Delferriere, J. Fils, Y. Gauthier, R. Hollinger, K. Knie, C.-M. Kleffner, and O. Tuske, "Status of high intensity proton injector for facility for antiproton and ion research," Rev. Sci. Instrum. 90, 123309 (2019).
- ²⁸W. Barth, A. Adonin, S. Appel, P. Gerhard, M. Heilmann, F. Heymach, R. Hollinger, W. Vinzenz, H. Vormann, and S. Yaramyshev, "Heavy ion linac as a high current proton beam injector," Phys. Rev. Spec. Top.-Accel. Beams 18, 050102 (2015).
- ²⁹ A. Adonin, W. Barth, F. Heymach, R. Hollinger, H. Vormann, and A. Yakushev, "Production of high current proton beams using complex H-rich molecules at GSI," Rev. Sci. Instrum. 87, 02B709 (2016).
- ³⁰F. Herfurth, Z. Andelkovic, W. Barth, W. Chen, L. A. Dahl, S. Fedotova, P. Gerhard, M. Kaiser, O. K. Kester, H.-J. Kluge *et al.*, "The HITRAP facility for slow highly charged ions," Phys. Scr. **T166**, 014065 (2015).
- ³¹S. Busold, A. Almomani, V. Bagnoud, W. Barth, S. Bedacht, A. Blažević, O. Boine-Frankenheim, C. Brabetz, T. Burris-Mog, T. E. Cowan *et al.*, "Shaping laser accelerated ions for future applications—The LIGHT collaboration," Nucl. Instrum. Methods Phys. Res., Sect. A 740, 94–98 (2014).
- ³²S. Yaramyshev, K. Aulenbacher, W. Barth, M. Basten, M. Busch, V. Gettmann, M. Heilmann, T. Kuerzeder, M. Miski-Oglu, H. Podlech *et al.*, "Advanced approach for beam matching along the multi-cavity SC CW linac at GSI," J. Phys.: Conf. Ser. 1067, 052005 (2018).
- ³³P. Gerhard, W. Barth, L. Dahl, A. Orzhekhovskaya, K. Tinschert, W. Vinzenz, H. Vormann, and S. Yaramyshev, "Commissioning of a new CW radio frequency quadrupole at GSI," in *Proceedings of IPAC'10* (IPAC'10 OC/ACFA, 2010), pp. 741–743; available at https://accelconf.web.cern.ch/IPAC10/.
 ³⁴U. Ratzinger, Effiziente Hochfrequenz-Linearbeschleuniger für Leichte und
- ⁵⁴U. Ratzinger, Effiziente Hochfrequenz-Linearbeschleuniger für Leichte und Schwere Ionen (IAP, Goethe University, Frankfurt am Main, Germany, 1998), habilitation.
- ³⁵R. Tiede, U. Ratzinger, H. Podlech, C. Zhang, and G. Clemente, "KONUS beam dynamics designs using H-mode cavities," in *Proceedings of HB'08* (2008); available at https://www.researchgate.net/publication/23403 5056_KONUS_beam_dynamics_designs_using_H-mode_cavities pp. 223–230.
- ³⁶I. Pinayev, Y. Jing, D. Kayran, V. N. Litvinenko, J. Ma, K. Mihara, I. Petrushina, K. Shih, G. Wang, and Y. H. Wu, "Using solenoid as multipurpose tool for measuring beam parameters," Rev. Sci. Instrum. 92, 013301 (2021).
- ³⁷S. Lauber, K. Aulenbacher, W. Barth, F. Dziuba, J. List, C. Burandt, V. Gettmann, T. Kürzeder, M. Miski-Oglu, P. Forck *et al.*, "Longitudinal phase space reconstruction for a heavy ion accelerator," Phys. Rev. Accel. Beams 23, 114201 (2020).
- ³⁸O. Brunner, S. Calatroni, E. Ciapala, M. Eshraqi, R. Garoby, F. Gerigk, A. Lombardi, R. Losito, V. Parma, C. Rossi *et al.*, "Assessment of the basic

- parameters of the CERN superconducting proton linac," Phys. Rev. Spec. Top.-Accel. Beams 12, 070402 (2009).
- ³⁹ V. Palmieri, A. M. Porcellato, V. L. Ruzinov, S. Y. Stark, L. Badan, A. Beltramin, L. Bertazzo, R. Preciso, F. Stivanello, G. Bisoffi, L. Boscagli *et al.*, "Installation in the LNL ALPI linac of the first cryostat with four niobium quarter wave resonators," Nucl. Instrum. Methods Phys. Res., Sect. A **382**, 112–117 (1996).
- ⁴⁰B. Walasek-Hoehne, B. Walasek-Hoehne, C. Andre, P. Forck, E. Guetlich, G. Kube, P. Lecoq, and A. Reiter, "Scintillating screen applications in accelerator beam diagnostics," IEEE Trans. Nucl. Sci. 59, 2307–2312 (2012).
- ⁴¹P. Forck, "Minimal invasive beam profile monitors for high intense hadron beams," in *Proceedings of IPAC'10* (IPAC'10 OC/ACFA, 2010), pp. 1261–1265; available at https://accelconf.web.cern.ch/IPAC10/.
- ⁴²T. Giacomini, S. Barabin, P. Forck, D. Liakin, and V. Skachkov, "Development of residual gas profile monitors at GSI," AIP Conf. Proc. 732, 286–293 (2004).
- ⁴³T. Sieber, W. Barth, P. Forck, V. Gettmann, M. Heilmann, H. Reeg, A. Reiter, and S. Yaramyshev, "Bunch shape measurements at the GSI CW-linac prototype," in *Proceedings of IPAC'18* (JACoW Publishing, Geneva, Switzerland, 2018), pp. 2091–2094; avialable at https://accelconf.web.cern.ch/ipac2018/.
- ⁴⁴A. Feschenko, "Methods and instrumentation for bunch shape measurements," in *Proceedings of PAC'01* (IEEE, 2001), pp. 517–521; available at https://ieeexplore.ieee.org/document/987557.
- ⁴⁵B. Ledroit and K. Aulenbacher, "Collimation of target induced halo following MAGIX at MESA," J. Phys.: Conf. Ser. 1350, 012138 (2019).
- ⁴⁶V. Rizzoglio, A. Adelmann, C. Baumgarten, M. Frey, A. Gerbershagen, D. Meer, and J. M. Schippers, "Evolution of a beam dynamics model for the transport line in a proton therapy facility," Phys. Rev. Accel. Beams **20**, 124702 (2017).
- ⁴⁷L. Arnaudon, O. Aberle, R. Assmann, J. Bacher, V. Baglin, G. Bellodi, A. Bertarelli, P. Bestmann, R. Billen, V. Boccone *et al.*, "Linac4 technical design report," Technical Report CERN-AB-2006-084, CERN, 2006.
- ⁴⁸R. Miyamoto, H. Danared, M. Eshraqi, and A. Ponton, "Numerical study of a collimation system to mitigate beam losses in the ESS linac," in *Proceedings of IPAC'12*, 2012.
- ⁴⁹M. Yarmohammadi Satri, A. M. Lombardi, and F. Zimmermann, "Multiobjective genetic algorithm approach to optimize beam matching and beam transport in high-intensity hadron linacs," Phys. Rev. Accel. Beams 22, 054201 (2019).
- ⁵⁰ V. A. P. Aguiar, N. H. Medina, N. Added, E. L. A. Macchione, S. G. Alberton, A. R. Leite, F. R. Aguirre, R. V. Ribas, C. C. Perego, L. M. Fagundes *et al.*, "SAFIIRA: A heavy-ion multi-purpose irradiation facility in Brazil," Rev. Sci. Instrum. 91, 053301 (2020).
- ⁵¹O. Romanenko, V. Havranek, A. Mackova, M. Davidkova, M. Cutroneo, A. G. Ponomarev, G. Nagy, J. Stammers, and I. Rajta, "Performance and application of heavy ion nuclear microbeam facility at the Nuclear Physics Institute in Řež, Czech Republic," Rev. Sci. Instrum. 90, 013701 (2019).
- ⁵²S. Yaramyshev, W. Barth, L. Groening, A. Kolomiets, and T. Tretyakova, "Development of the versatile multi-particle code DYNAMION," Nucl. Instrum. Methods Phys. Res., Sect. A 558, 90–94 (2006).
- ⁵³ M. Miski-Oglu, M. Amberg, K. Aulenbacher, and V. Gettmann, "Steps towards superconducting CW-LINAC for heavy ions at GSI," in Proceedings of SRF'15, 2015.
- ⁵⁴F. Gao and L. Han, "Implementing the Nelder-Mead simplex algorithm with adaptive parameters," Comput. Optim. Appl. **51**, 259–277 (2012).
- 55 See www.cst.com for CST MicroWave Studio; accessed 21 July 2021.
- ⁵⁶G. Riehl, J. Pozimski, W. Barth, and H. Klein, "A multi-functional profile and emittance measurement system," in *Proceedings of EPAC'90* (Editions Frontières, 1990); available at https://isbnsearch.org/isbn/2863320904 pp. 756–757.